# Quantitative analysis of amino acid metabolism in liver cancer links glutamate excretion to nucleotide synthesis

Avlant Nilsson[a,1], Jurgen R. Haanstra[b,1], Martin Engqvist[a], Albert Gerding[c,d], Barbara M. Bakker[b,c], Ursula Klingmüller[e], Bas Teusink[b], and Jens Nielsen[a,f,2]

[a]Department of Biology and Biological Engineering, Chalmers University of Technology, SE41296 Gothenburg, Sweden; [b]Systems Biology Lab, Amsterdam Institute of Molecular and Life Sciences (AIMMS), Vrije Universiteit Amsterdam, NL1081HZ Amsterdam, The Netherlands; [c]Laboratory of Pediatrics, Systems Medicine of Metabolism and Signaling, University of Groningen, University Medical Center Groningen, NL-9713AV Groningen, The Netherlands [d]Department of Laboratory Medicine, University of Groningen, University Medical Center Groningen, NL-9713AV Groningen, The Netherlands; [e]Division of Systems Biology and Signal Transduction, German Cancer Research Center, D-69120 Heidelberg, Germany; and [f]Novo Nordisk Foundation Center for Biosustainability, Technical University of Denmark, Kongens Lyngby, DK2800, Denmark

Contributed by Jens Nielsen, March 9, 2020 (sent for review November 4, 2019; reviewed by Eytan Ruppin and Matthew G. Vander Heiden)

**Many cancer cells consume glutamine at high rates; counterintuitively, they simultaneously excrete glutamate, the first intermediate in glutamine metabolism. Glutamine consumption has been linked to replenishment of tricarboxylic acid cycle (TCA) intermediates and synthesis of adenosine triphosphate (ATP), but the reason for glutamate excretion is unclear. Here, we dynamically profile the uptake and excretion fluxes of a liver cancer cell line (HepG2) and use genome-scale metabolic modeling for in-depth analysis. We find that up to 30% of the glutamine is metabolized in the cytosol, primarily for nucleotide synthesis, producing cytosolic glutamate. We hypothesize that excreting glutamate helps the cell to increase the nucleotide synthesis rate to sustain growth. Indeed, we show experimentally that partial inhibition of glutamate excretion reduces cell growth. Our integrative approach thus links glutamine addiction to glutamate excretion in cancer and points toward potential drug targets.**

genome-scale modeling | flux-balance analysis | systems biology | metabolic engineering

Cancer cell metabolism transcends the hallmark Warburg effect (1), where glucose consumption is increased and lactate is excreted under aerobic conditions. Most carbon in cancer cells originates from amino acids (2) that are either taken up directly from the environment or synthesized de novo in the case of some nonessential amino acids. While amino acids are incorporated into biomass at rates that depend on the amino acid composition of the cell and the growth rate (3), some amino acids, most notably glutamine, are consumed at rates markedly exceeding what is required for protein synthesis (4); simultaneously, several other amino acids are excreted, e.g., glutamate, proline, alanine, and glycine (5, 6). It seems puzzling that glutamate excretion, which has been observed to correlate with growth rate and aggressiveness in xenografts (7), co-occurs with glutamine uptake; a mere conversion of glutamine to glutamate would only result in net import of ammonium, and yet cells excrete nitrogen both directly as ammonium (8) and indirectly as alanine (5). Despite many studies on the importance of metabolic fluxes for cancer cell proliferation, we still lack an integrative view of how cells coordinate acquisition of the diverse nutrients required for growth (9). A systems-level analysis is required to understand the interplay between amino acids and growth in cancer cells.

Mathematical models are indispensable to attain a systems-level understanding of cancer cell metabolism. Many insights into cancer metabolism have been achieved through such models, e.g., the importance of glutamine as a free-energy source (10), the role of one carbon metabolism in reduced nicotinamide-adenine dinucleotide phosphate (NADPH) balance (11), and how the uptake of metabolites in excess of biosynthetic demands correlate with the excretion of lactate, glutamate, alanine, and glycine (5). However, a full genome-wide modeling approach is required to expand our knowledge of how metabolism functions beyond the canonical pathways and, in particular, to understand the intricate effects of metabolic compartmentalization and the interplay between exchange fluxes and synthesis of biomass. A platform for this type of analysis are genome-scale metabolic models (GEMs) that are a mathematical formalization of all known metabolic reactions of an organism (12). Human cell type-specific models have been developed based on proteomics or RNA sequencing data to include only reactions catalyzed by expressed proteins in the studied cell type and also include information of cellular compartments (13). Such models provide a comprehensive and quantitative analysis of metabolism and have been extensively used in the study of metabolism in microorganisms (14), as well as in mammals, e.g., metabolism in infants (15), muscle cells (16), and Chinese hamster ovary

## Significance

**We used a combination of experimental measurements and computer simulations to understand how liver cancer cells rewire their metabolism to grow faster. We observed that glutamate is excreted by the cells, and our simulations suggest that this occurs because glutamate is formed in excess in the cytoplasm, when cells rapidly synthesize nucleotides, which are required for growth. Meanwhile, glutamate that is formed in the mitochondria is, on the other hand, not excreted. Treating glutamate as two distinct pools, a cytosolic and a mitochondrial, is useful to better understand why many cancer cells rapidly consume glutamine, the precursor of glutamate. The results point toward potential drug targets that could be used to reduce growth of liver cancer cells.**

Author contributions: A.N., J.R.H, U.K., B.T., and J.N. designed research; A.N, J.R.H., and A.G. performed research; A.N. and M.E contributed new reagents/analytic tools, A.N. and J.R.H. analyzed data; and A.N, J.R.H., M.E., B.M.B., B.T., and J.N. wrote the paper.

Reviewers: E.R., National Cancer Institute; and M.G.V.H., Koch Institute at the Massachusetts Institute of Technology.

The authors declare no competing interest.



Data deposition: Raw data are available in the online repository FAIRDOMHub (DOI: 10.15490/fairdomhub.1.investigation.369.2). The model and the source code for the computational methods are available at GitHub (https://github.com/SysBioChalmers/LiverCellMetabolismSimulation).

[1]A.N. and J.R.H. contributed equally to this work.

[2]To whom correspondence may be addressed. Email: nielsenj@chalmers.se.

This article contains supporting information online at https://www.pnas.org/lookup/suppl/doi:10.1073/pnas.1919250117/-/DCSupplemental.

First published April 27, 2020.

cells (17); yet they have not been used to their full potential in the study of cancer metabolism (18). So far, genome-scale metabolic models of cancer have either been nonquantitative or relied on published data that were collected for other purposes. It can be anticipated that modeling results with better precision can be obtained when data are collected with a specific purpose in mind.

Quantitative analysis of metabolism requires time-resolved data. It is important to ensure that the data to be analyzed are obtained from well-defined steady-state growth phases and that the metabolite measurements allow a proper estimate of exchange fluxes between cells and the growth medium. We have previously shown that this can be a challenge for metabolic-profiling studies with limited temporal resolution, due to metabolite depletion (19). To be able to quantify the specific growth rate, the cultivation time must be sufficiently long to allow detectable changes in cell counts, i.e., one or more doublings. However, to allow metabolite concentrations to be quantified over time, the medium cannot be replenished during the cultivation. This setup may therefore result in depletion of growth-enhancing metabolites during the cultivation that sections growth into multiple growth phases. Since each phase has a unique flux profile and growth rate, the analysis may be compromised if these are not studied independently (19).

Liver cancer is particularly relevant in the study of amino acid metabolism. The healthy liver is a hub for amino acid metabolism in the human body, and the metabolic capabilities of the healthy liver are likely carried over to malignant cells since a strong correlation exists between the molecular signatures of cancers and their tissues of origin (20, 21). In the healthy liver, the role of amino acid metabolism is affected by the nutritional status of the body as the liver also plays an important role in whole-body glucose homeostasis. As liver cells therefore experience different levels of glucose, it is also relevant to study amino acid metabolism under varying concentrations of glucose. In addition, this may mimic the situation in solid tumors, where the glucose concentration depends on the distance from disorganized and leaky blood vessels (22).

Here, we measure cell proliferation and medium metabolite levels of glucose, pyruvate, lactate, and amino acids over time at different glucose levels and identify a period of steady-state growth. We use a metabolic model to integrate data and find that a large share of the glutamine consumed by the cells is metabolized in the cytosol to support biosynthetic processes, the synthesis of nucleotides in particular. The model reveals that this, together with deamination of branched-chain amino acids (BCAAs), is the major source of cytosolic glutamate, which is subsequently excreted by the cells. Hypothesizing that glutamate excretion is linked to biosynthesis, we partially blocked glutamate excretion and observed a reduction in growth. We additionally performed a sensitivity analysis to identify other potential drug targets. Altogether, the present study demonstrates how a genome-scale metabolic model, together with a rigorous quantitative and time-resolved dataset, can be used to elucidate connections between fluxes, across compartments and the cell membrane in mammalian cells.

## Results

**Modeling Sectioned the Experiment into Growth Phases.** First, we set up a metabolic model specific for the liver cancer cell line HepG2. The model was based on the Human Metabolic Reaction database HMR 2.0, a generic GEM (23), from which reactions without support in RNA-sequencing (RNA-seq) count data had been removed (24). Manual curation of reactions relating to amino acid metabolism was performed and some additional reactions were introduced from an online database (Kyoto Encyclopedia of Genes and Genomes) (25). A biomass equation was developed for the model (*SI Appendix*, *Supplementary Methods*) with the specific amino acid composition of HepG2 cells as estimated from protein abundance data for HepG2 cells (26) and the amino acid frequency of these proteins (*SI Appendix*, Fig. S1).

Time-resolved data were acquired for cells in cultivation. Metabolite concentrations were quantified to infer the specific exchange fluxes (in micromoles per time per biomass unit) for HepG2 cells under different nutrient conditions (all metabolite measurements are available in Dataset S1). Cells were cultivated in a Dulbecco's modified Eagle medium (DMEM)-based medium with addition of different levels of glucose (0, 6, or 22 mM) and 10% fetal calf serum (FCS). Cells where cultivated for 6 d, and samples were taken at multiple time points. An initial set of measurements were performed to identify a time interval during which the cells where in steady state, where fluxes can be well defined and are amenable to genome-scale metabolic modeling. We measured the amino acid concentrations with a single replicate at 0, 23, 48, 78, and 144 h. At 144 h, most of the cells had died, and most metabolites were depleted, so this time point was excluded from further analysis.

The cultivations underwent several growth phases. To clearly distinguish them, we developed a simplified version of an existing modeling approach (27), here referred to as piece-wise flux-balance analysis (pwFBA) (*Methods*). Using pwFBA, the cultivations were found to undergo four distinct metabolic phases (Fig. 1); the triggering events involved depletion of metabolites, e.g., glucose and glutamine, but we also found it warranted to introduce a new phase once glutamine levels dropped below 1.2 mM, as this coincided with a transition to stabilized pyruvate levels (*SI Appendix*, Fig. S2). Additionally, we made use of pwFBA to assess whether vitamins or cofactors could become limiting during the cultivation, which has been observed in other studies (19); the analysis suggested that choline and pantothenate were close to depletion toward the end of the cultivation, based on their initial concentrations in the cultivation medium and their specific consumption rates (*SI Appendix*, Fig. S3).

We inspected the phases to select a suitable candidate for in-depth analysis. The pwFBA approach revealed rapid exchange fluxes for some metabolites during the first hours of cultivation, including glutamine, pyruvate, alanine, and glutamate (*SI Appendix*, Fig. S2). We decided to not select this phase for further analysis since it was too short to attain accurate growth estimates, and since some of the exchange fluxes required to close its carbon balance were tentative, e.g., excretion of proteins (*SI Appendix*, *Supplementary Methods*). The pwFBA further showed that both glutamine and glucose were depleted over the course of the cultivation, after which the cells continued to grow at a reduced rate. We found that glutamine depletion, rather than glucose depletion, was the primary cause of growth reduction, since a similar reduction in growth was observed also when glucose was still available in excess (22 mM initial glucose). This was consistent with the observation that the cells were able to grow in near-absence of glucose (0 mM initial glucose), albeit slower compared to cultures with glucose available (Fig. 1). We noticed that the flux of alanine changed direction from excretion to consumption after glutamine was depleted, which is in agreement with flux studies of HepG2 cells grown in the absence of glutamine, where alanine consumption is also observed (28). It is likely that alanine substitutes glutamine as a nitrogen source once it is depleted, as noted by others (29). Taken together, the balanced phase that followed directly after the initial rapid phase was found to be most suitable for further in-depth study, as no metabolites were depleted and it had robust growth at steady state with well-defined fluxes.

**Amino Acids Are Diverted from Protein Synthesis.** The fluxes in the balanced growth phase were characterized with higher precision. We measured amino acid concentrations in biological triplicates from samples taken at 23, 30, and 48 h for each condition and

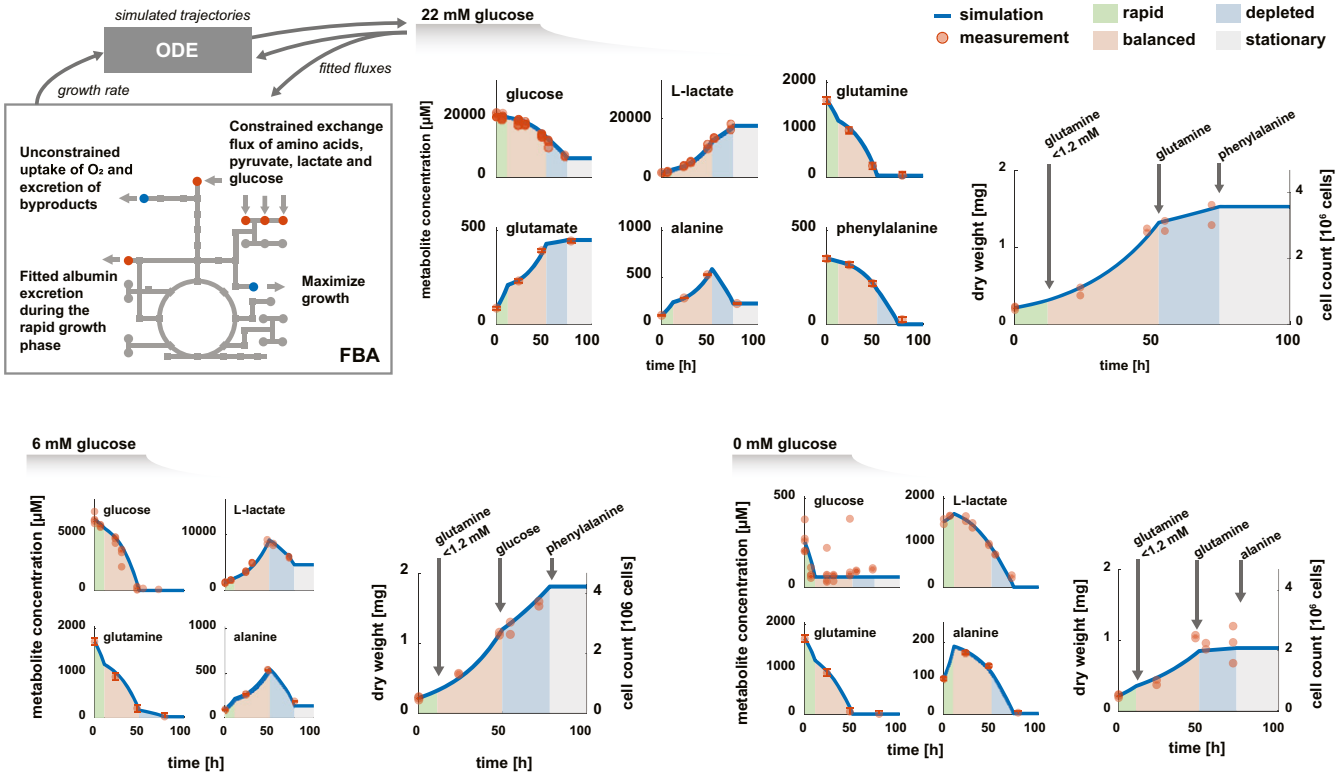


**Fig. 1.** Time-resolved exometabolome measurements were combined with metabolic modeling to identify well-defined growth phases. Metabolite concentrations were measured under three different conditions (0, 6, and 22 mM initial glucose). The metabolic model was constrained with tentative exchange fluxes, and the maximum attainable growth rate was predicted using FBA. The exchange fluxes and growth rates were used as input to an ODE system, to draw simulated metabolite and growth trajectories (blue lines) ensuring that the fitted exchange fluxes would be consistent with the experimental measurements (filled orange circles) of metabolite concentrations and cell counts. The ODE model was configured to take into account the increasing number of cells, changes in culture medium volume due to sample removal, and spontaneous degradation of glutamine. It was set up to automatically switch to a new growth phase (indicated by shading) using a new set of exchange fluxes when metabolic events occurred such as metabolite depletion (indicated by arrows in the growth curves). The exchange fluxes for each phase were manually adjusted until there was agreement between simulations and measurements. Glucose, lactate, and cell counts were measured in several biological replicates, and each measurement is shown independently. Amino acids were measured as single replicates, and the error bar shows the technical error, estimated from the SD of six independent measurements at time 0. In the 0 mM glucose condition, there was some residual glucose from the FCS in medium.

quantified the exchange fluxes and their 95% CI (Fig. 2*A*) using the maximum log likelihood (mLL) method (30) (*Methods* and *SI Appendix*, Fig. S4). Most fluxes were in quantitative agreement among the studied conditions and in qualitative agreement with observations in other cell lines (3, 5). For cultures with 0 mM initial glucose, alanine was not excreted and the rate of glycine excretion was markedly increased; the cells also had a higher estimated glutamine consumption rate. The predicted growth under this condition was in the lower range of the measurements, which could indicate that the measured growth rate was overestimated, e.g., due to variability in the cell counts; the predicted growth was underestimated, e.g., due to underestimating some of the measured uptake fluxes; or that utilization of unmeasured carbon sources was important under this condition, e.g., metabolism of proteins. For cultures with 6 and 22 mM initial glucose, the growth predictions were in good agreement with the measurements, indicating that most fluxes were characterized with high precision.

To map out which amino acids required further attention, we compared their exchange fluxes to their abundance in biomass, which was calculated from the amino acid content in protein (*SI Appendix*, Fig. S1) and the concentration of free amino acids. The uptake of glutamine greatly exceeded the requirements, and there was also higher-than-required consumption of branched chain amino acids, phenylalanine, arginine, and cystine (Fig. 2*B*). Simultaneously, glutamate, alanine, and proline were excreted to the medium, implying that production of these metabolites was higher than required for growth. The uptake of serine was in reasonable agreement with the demand for protein synthesis (Fig. 2*B*), which is in contrast to observations in many other cell lines, where it is overconsumed (3). We were interested to find the connections between amino acids that were overconsumed and the ones that were produced through the highly interconnected metabolic network. To find metabolic connections between the amino acids, we developed an algorithm termed GEMpress (*SI Appendix*, Fig. S5) that compresses the metabolic network to only include metabolites that are at branch points. We could then find connections between consumed and produced amino acids using a shortest path algorithm.

Using GEMpress, we found that most metabolites were interconnected via glutamate, with some noteworthy exceptions. Glutamate was a hub metabolite for glutamine, the branched chain amino acids, alanine, proline, as well as aspartate and asparagine (*SI Appendix*, Fig. S5). One exception was consumption of phenylalanine that was directly connected to tyrosine production via the liver-specific enzyme phenylalanine-4-hydroxylase (PAH). This reaction potentially supports the cancer through recharging the electron transmitter tetrahydrobiopterin, which is linked to liver cancer in mice (31). Another exception was synthesis of glycine; while glycine can be synthesized from serine, the uptake of serine was well-balanced, and de novo synthesis of serine would be required. Simulations (*SI Appendix*,

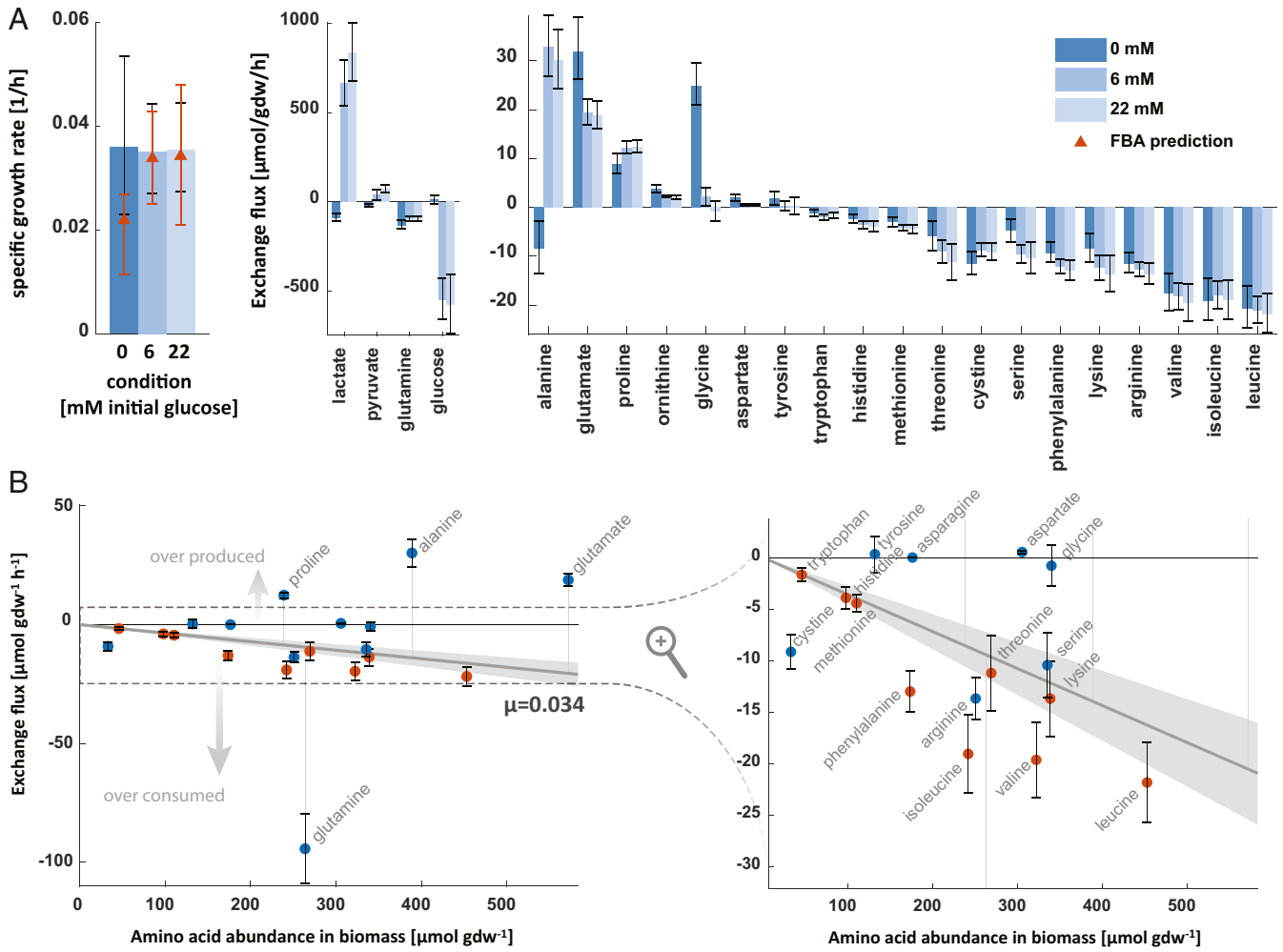


**Fig. 2.** Estimation and analysis of exchange fluxes in the balanced growth phase. (*A*) mLL estimates of specific growth rates and fluxes and their 95% CIs. Fluxes were estimated from metabolite concentrations in biological triplicates at 23, 30, and 48 h. Growth was estimated from cell counts in duplicates at 23 and 48 h, counts from the 6 and 22 mM condition were pooled to improve power, and the counts at 48 and 55 h were pooled for the 0 mM condition. The FBA prediction of specific growth rate used the estimated fluxes as input; the upper and lower bounds were calculated using the upper and lower bound of the fluxes, respectively; fluxes were omitted if their CI overlapped zero. (*B*) The requirement of amino acids for growth depends on the growth rate (gray line, 95% CI as shaded area) and the amino acid abundance in biomass (protein bound amino acids + the free amino acid pool). If the uptake rate is higher than the incorporation rate, then the amino acid is metabolized; if the uptake rate is lower, then the amino acid must be produced by some other process to meet the biosynthetic demand. Essential amino acids (orange circles) cannot be produced and must be consumed at rates at least as high as the requirement for growth. For cystine, the amino acid abundance in biomass has been divided by two since cysteine (cyc) participates in biomass, while cystine (a cyc-cyc conjugate) is provided in the medium. Data are from the 22 mM glucose condition.

Fig. S5) suggested that glycine may instead be synthesized through the enzyme alanine-glyoxylate aminotransferase (AGTX), a protein that is particularly abundant in HepG2 cells (32). This may, via glyoxalate, support cancer growth through metabolic connections to NADPH, which is a role previously shown for synthesis of glycine through other pathways (11).

**Glutamate Excretion Is Linked to Biosynthetic Processes.** We analyzed the intracellular fluxes surrounding the hub metabolite glutamate. To obtain a quantitative understanding of its interconversion to other amino acids, the intracellular fluxes were investigated, taking metabolic compartmentalization into account. To analyze how the certainty of these fluxes were affected by experimental uncertainty and pathway redundancy, we applied flux-variability analysis (FVA) and found substantial uncertainty for most fluxes (predicted fluxes and variability estimates are provided in Dataset S2). We were able to partially circumvent this by constraining the uptake fluxes strictly to their best fit values, and the specific growth rate to the predicted maximum rate, which prevented adenosine triphosphate (ATP)-expending futile cycles, although this could potentially result in underestimated variability for reactions where such cycles do occur. The variability from cycles was further reduced by analyzing the net flux of groups of reactions with the same biological function, e.g., transport of glutamate into the mitochondria by multiple reactions. Relaxing the constraints of the exchange fluxes to cover the 95% CI of the fluxes resulted in almost complete uncertainty for most fluxes, except for those involved in biosynthesis and BCAA metabolism, which remained robust (*SI Appendix*, Fig. S6).

More than 60% of the glutamine is metabolized in the mitochondria (Fig. 3*A*). There it is converted to glutamate by the mitochondrial enzyme glutaminase (GLS). It is then further metabolized to alpha-ketoglutarate (AKG) through transamination reactions forming alanine and aspartate. The synthesis of these amino acids covers their biosynthetic requirement, and in the case of alanine, the production largely exceeded it, resulting in excretion. As the alanine flux is reversed in the

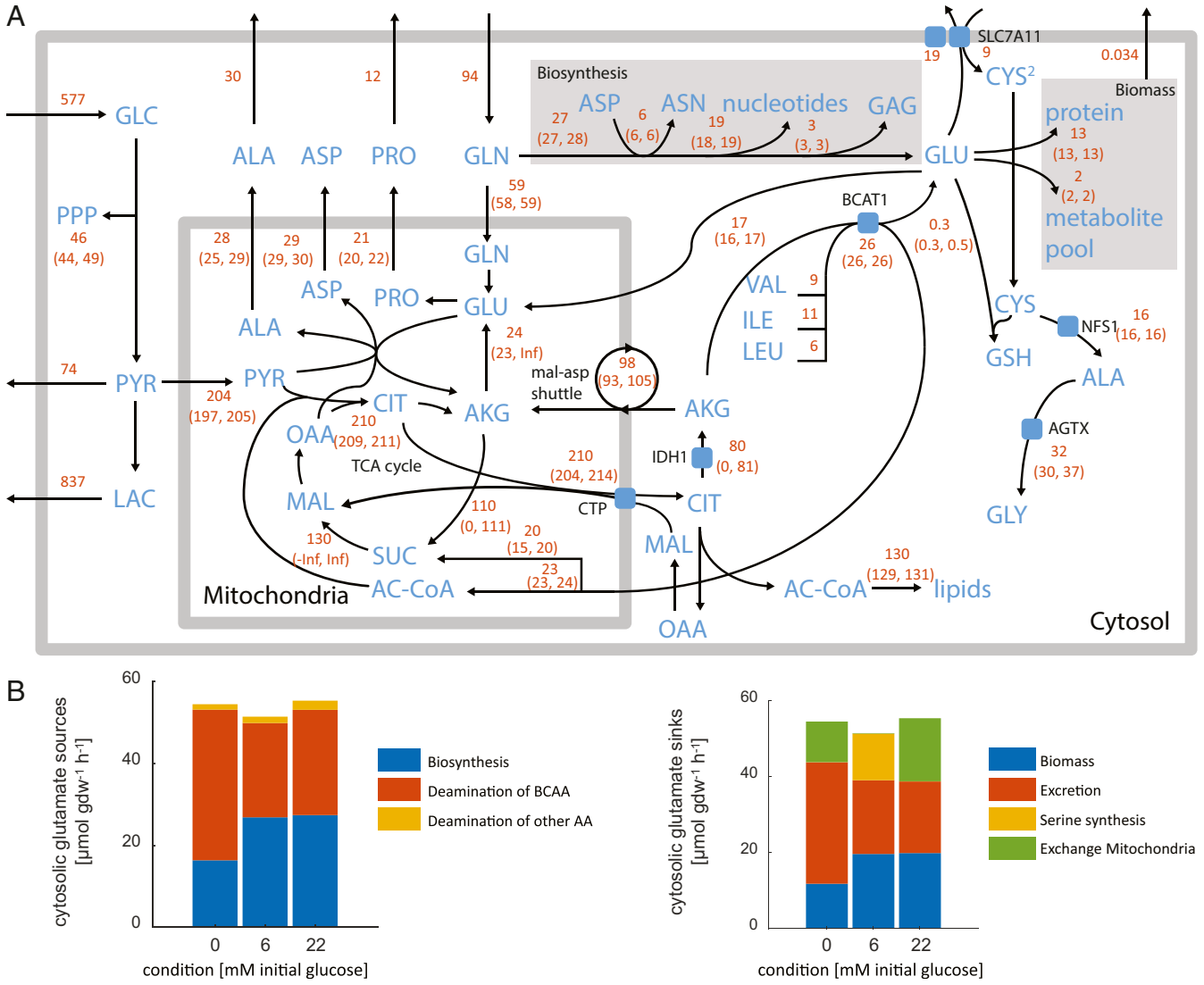


**Fig. 3.** Separation of glutamine (GLN) metabolism into a cytosolic and mitochondrial pool. (*A*) The major carbon fluxes (μmol gdw$^{-1}$ h$^{-1}$) during the balanced phase with 22 mM initial glucose. The fluxes are pwFBA predictions from constraining the exchange fluxes to their mLL estimates and constraining growth to the predicted maximum growth rate. Values in parenthesis correspond to the lower and upper bound using FVA. For several linear pathways, the reactions have been lumped from input to end product, e.g., metabolism of branched chain amino acids, and for metabolites that participate in cycles several reactions have been grouped to only show the net flux, e.g., the transport of glutamate into the mitochondria does not include the cycling of glutamate due to the malate-aspartate cycle. The flux to biomass from cytosolic amino acids is only indicated in the case of GLU and cytosolic ALA is shown in two locations to avoid overlapping lines. (*B*) The flux balance of the sources and sinks of cytosolic glutamate shows that deamination of BCAA is the quantitatively most significant source. AC-CoA, acetyl-coenzyme A; ASN, asparagine; ASP, aspartate; CYS, cysteine; CYS2, cystine; GAG, glycosaminoglycan; GLC, glucose; GLU, glutamate; GLY, glycine; ILE, isoleucine; LAC, lactate; LEU, leucine; MAL, malate; OAA, oxaloacetate; PPP, pentose phosphate pathway; PRO, proline; PYR, pyruvate; SER, serine; SUC, succinate; VAL, valine.

absence of glucose (Fig. 2*A*), this suggests that the alanine excretion is a byproduct of mitochondrial AKG production in the presence of excess pyruvate. Requirements for mitochondrial AKG can thus explain the metabolic benefit of these fluxes. The benefit of proline synthesis from glutamine remains intriguing, although it may be linked to its role in mitochondrial NADPH oxidation, which has been proposed as an explanation by previous studies (33).

Nearly 30% of the glutamine is metabolized in the cytosol besides the 8% that goes into biomass. There it donates one nitrogen in the biosynthesis of nucleotides to form glutamate. This also occurs in the formation of asparagine from aspartate and in synthesis of glycosaminoglycans. Taken together, these biosynthetic reactions are the source of roughly half of the cytosolic glutamate (Fig. 3*B*). Deamination of BCAAs is the second major source, which has been confirmed in other cell lines, where 40% of the glutamate became labeled from $^{15}$N-labeled BCAA (34). The metabolism of BCAA is also linked to growth, as knocking down the BCAA aminotransferase (BCAT) has been shown to reduce growth markedly (34). We were, however, unable to find a direct metabolic explanation for this effect (*SI Appendix*, *Supplementary Methods*), and it is possible that the growth reduction acts via a role of BCAAs in signaling. It has been hypothesized that the consumption of AKG by the transamination of BCAA may lower cytosolic AKG levels and stabilize the transcription factor HIF-1α through substrate depletion (34). However, in our simulations, the AKG required for BCAA metabolism mostly originated from mitochondrial citrate (Fig. 3*A*) that was transported to the cytosol and converted into AKG through isocitrate dehydrogenase (IDH1).

Therefore, an alternative possibility may be that increased flux through IDH1 increases byproduction of 2-hydroxyglutarate, a metabolite that is linked to cancer (35).

We find a connection between the synthesis and excretion rate of cytosolic glutamate. The net flux of carbon between the cytosolic and the mitochondrial glutamate pool is comparably low (Fig. 3*B*), and the observed excretion rate of glutamate corresponds well to the surplus of glutamate formed by transamination activities, including nucleotide synthesis, in the cytosol. This suggests that cells excrete glutamate that is formed in excess in the cytosol. This is in agreement with observations in other cell lines, where glutamate production is reduced from knocking down BCAT (36). It should be noted that even though there is significant mixing of the cytosolic and mitochondrial glutamate pool due to the aspartate–malate shuttle, the net flux of glutamate between cytosol and mitochondrion is low. The reason is that the shuttle functions to transport cytosolic reduced nicotinamide-adenine dinucleotide (NADH) to the mitochondria but, importantly, does not transport carbon when fully balanced. Only an imbalanced shuttle allows the export of aspartate from the mitochondria for biosynthetic purposes in exchange for cytosolic glutamate. The metabolic benefit of glutamate excretion is thus that it allows for continuous transamination activities in the cytosol: without this sink, glutamate would accumulate and block further flux.

**Inhibition of Glutamate Excretion Reduces Growth.** We hypothesized that cellular excretion of glutamate is essential for the cells to ensure high-level supply of nucleotides that is required for high specific growth rate and flux through BCAT that has been demonstrated (34) to support growth. We thus expected that growth would decrease in response to inhibited glutamate excretion since the flux through these reactions would have to be reduced in the absence of glutamate excretion as a sink to balance the flux. This would be in agreement with literature studies that show attenuated growth in xenograft models when the glutamate transporter is knocked out (37). Since excretion constitutes around 45% of the total sink of cytosolic glutamate (Fig. 3*B*), complete inhibition could be expected to cause a corresponding 45% reduction in growth, but this would also depend on the effects on BCAT and mitochondrial exchange.

Because our simulations rely on measured exchange fluxes, they cannot readily be extended to investigate counterfactual conditions such as glutamate inhibition. In an attempt to extrapolate the simulations, we constrained the fluxes to not surpass the predicted optimal level and investigated the effect of glutamate inhibition in this scenario (*SI Appendix*, Fig. S9). Under the assumption that the predicted flux is close to the effective capacity of the enzymes, this can be viewed as emulating enzyme capacity constraints, which have been shown to be predictive of metabolic phenotypes in cancer in previous studies (38). The extrapolated simulations suggested that inhibited glutamate excretion would reduce growth through reduced nucleotide synthesis, conditioned that mitochondrial exchange does not increase and flux through BCAT is unaffected. The extrapolation further suggests that there would be no synergistic effects from inhibiting both glutamine uptake and glutamate excretion, and that it would be infeasible to sustain high levels of glutamate excretion in the absence of glutamine, which is in agreement with experimental observations (29).

To further corroborate our hypothesis, we inhibited glutamate export experimentally. The export of glutamate can be inhibited by the drug sulfasalazine (SSZ), which targets the glutamate/cystine antiporter SLC7A11 (37, 39) (cystine is a cysteine–cysteine conjugate). We cultivated cells with 0, 0.1, and 0.2 mM SSZ, and both uptake of cystine (Fig. 4*A*), release of glutamate (Fig. 4*B*), and the specific growth rate (Fig. 4*C*) were decreased in a dose-dependent manner. We were unable to completely inhibit the glutamate excretion due to solubility constraints of the drug. Besides, since more than twice as much glutamate is released compared to cystine consumed (Fig. 2*A*), there may also be other transporters engaged in glutamate export that we were unable to target. Overall, the reduction in flux was around 50% at the highest dose, while the reduction in specific growth rate was around 20%. This was in line with the expectation that a 100% reduction in glutamate excretion would result in a 45% growth reduction.

Most research on SLC7A11 focuses on its role in uptake of cystine (37, 39). Cystine can be converted to cysteine that plays a role in de novo synthesis of glutathione (GSH), which is an essential metabolite for management of oxidative stress. However, the GSH synthesis rate at 0.3 micromoles per gram dry weight (gdw) per hour (μmol $gdw^{-1}$ $h^{-1}$) only accounted for around 2% of the cystine flux observed in this study, based on an intracellular GSH concentration of 3.7 mM (40) that is consistent with targeted measurements of GSH in HepG2 cells at 3 mM (41). This suggests that the demand of GSH is not driving the flux through SLC7A11, and in our simulations most cysteine was degraded into alanine that was excreted (Fig. 3*A*). It should be noted that this occurred through a pathway that was introduced in the curation step because there was no apparent sink for cysteine in the draft model (*SI Appendix*, *Supplementary Methods*). The pathway involved cysteine desulfurase (NFS1) and persulfide dioxygenase (ETHE1) that are both over overexpressed in HepG2 compared to liver (*SI Appendix*, Fig. S7). It should further be noted that HepG2 cells have been reported to export intracellular GSH at rates corresponding to around 5% of

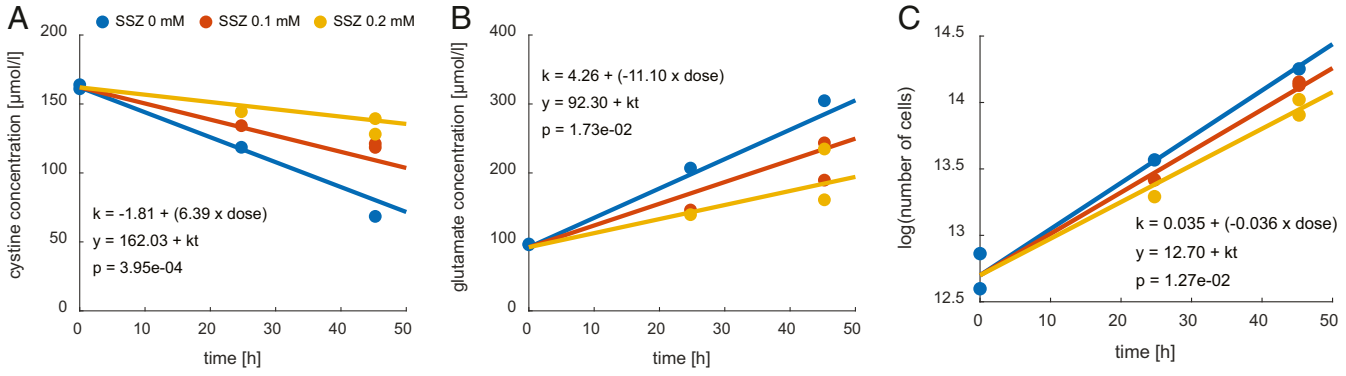


**Fig. 4.** Inhibition of glutamate excretion and reduction of growth by SSZ. Linear regression showed a dose-dependent decrease in cystine uptake (*A*), glutamate excretion (*B*), and specific growth rate (*C*) with increasing SSZ concentrations: 0 mM (blue), 0.1 mM (red), and 0.2 mM (yellow). There was no significant effect on other metabolites than cystine and glutamate, with the exception of a quantitatively small increase in asparagine excretion (*SI Appendix*, Fig. S8).

the total pool per hour (42), this would correspond to a flux in the order of 0.2 μmol $gdw^{-1}$ $h^{-1}$, corresponding to around 1% of the total cysteine flux. This was not included in the model.

**Growth Is Sensitive to Perturbations in Many Metabolic Reactions.** We used the metabolic model to identify other reactions that are essential for growth and thus can be potential drug targets. This has previously been done for liver cancer cells (13) and cell lines (24), but those studies relied on network topology and could only provide qualitative results (essential or nonessential). With our parametrized model, i.e., a model that describes a specific, well-defined steady state, we could give a more quantitative estimate of the sensitivity of growth in these states to a small reduction in flux through each reaction (Fig. 5). The analysis showed that reactions from pathways previously identified as essential also have high sensitivity. These reactions belong to linear pathways toward synthesis of biomass components, including nucleotide synthesis, and are often known targets of anticancer drugs, such as methotrexate (for pyridine metabolism) and statins (for cholesterol metabolism). De novo fatty acid synthesis is also an essential linear pathway that has previously been recognized as a therapeutic target (43). Our experimentally constrained metabolic model now points to additional metabolic pathways that should be further investigated for liver cancer drug targets.

## Discussion

In this study, we used a combination of experimental measurements and computer simulations to gain insight into the metabolic behavior of liver cancer cells during in vitro growth. Previous simulations of cancer metabolism have used reduced networks with all reactions in a single cell compartment (5, 11, 44). Here, we used a full genome-scale reconstruction of human metabolism and, instead, reduced the results to human readable form postsimulation. This allowed us to explore the full metabolic flexibility of the cells and allowed insights into operation of noncanonical pathways and the importance of compartmentalization. The separation of glutamine metabolism into its cytosolic and mitochondrial compartments, resolved the paradoxical observation that cells take up glutamine at high rates, transform it into glutamate, of which a large fraction is excreted; the model showed that glutamate is metabolized when formed in the mitochondria but excreted when formed in excess in the cytosol. Because all glutamine must pass through glutamate before being metabolized, this analysis illuminates an important aspect of glutamine addiction in cancer cells. The formation of cytosolic glutamate is coupled to biosynthetic reactions and metabolism of BCAA, which are both involved with growth, and may therefore explain the observed correlation between growth rate and glutamate excretion across different cancers (7). More research is, however, required to elucidate in which way metabolism of BCAAs contributes to growth.

We found that treating HepG2 cells with an inhibitor of the cystine–glutamate antiporter, SLC7A11, reduces their specific growth rate. This transporter is overexpressed in liver tumors compared to matched control tissue, and its expression is prognostic of survival (45). It is also overexpressed in several other cancers (46). It is commonly assumed that inhibition affects cells through decreased uptake of cystine (37, 47–49), which is thought to upset synthesis of GSH, rendering the cells vulnerable to oxidative stress. This is corroborated by observations that loss of viability at high inhibitor concentrations is rescued by addition of *N*-acetyl-cysteine or 2-mercaptoethanol (48, 49), which enables uptake of cysteine by the cells. However, at low inhibitor concentrations (≤0.2 mM), such as the ones used in the present study, these studies show limited effect on viability, and it appears that strong inhibition is required to affect GSH levels to a degree where viability is compromised. This is consistent with our quantitative analysis of cystine flux, where we find that around 3% of the measured cystine uptake is sufficient to support both GSH efflux and to maintain GSH levels in the growing cells, suggesting that near-complete inhibition is required to affect GSH levels. Our results suggest that reduced glutamate excretion may be of importance at intermediary levels of inhibition. Increased concentrations of glutamate in serum has been found in metabolic-profiling studies of liver cancer patients (50), consistent with studies in several other cancers (51, 52), although this may partially be due to systemic effects (53).

The inhibitor used in this study, SSZ, is known to inhibit several other targets, including nuclear factor kappa B signaling (54) and tetrahydrobiopterin biosynthesis (55). While we clearly demonstrate that it affects cystine uptake and glutamate excretion, we cannot exclude that the observed effects on growth also may be influenced by interactions with other targets. While the partial inhibition of the transporter attained in the present study did not completely abolish growth, also small reductions in exponential growth rate can potentially be of therapeutic value, but the usefulness would depend on how well healthy liver cells cope with inhibited glutamate export and/or cystine import. The inhibitor has recently been tested against tumors in mice and found particularly efficient as an adjuvant of other treatments (56, 57).

Other transporters than SLC7A11 must also be involved in glutamate excretion from the cell. This is apparent from the

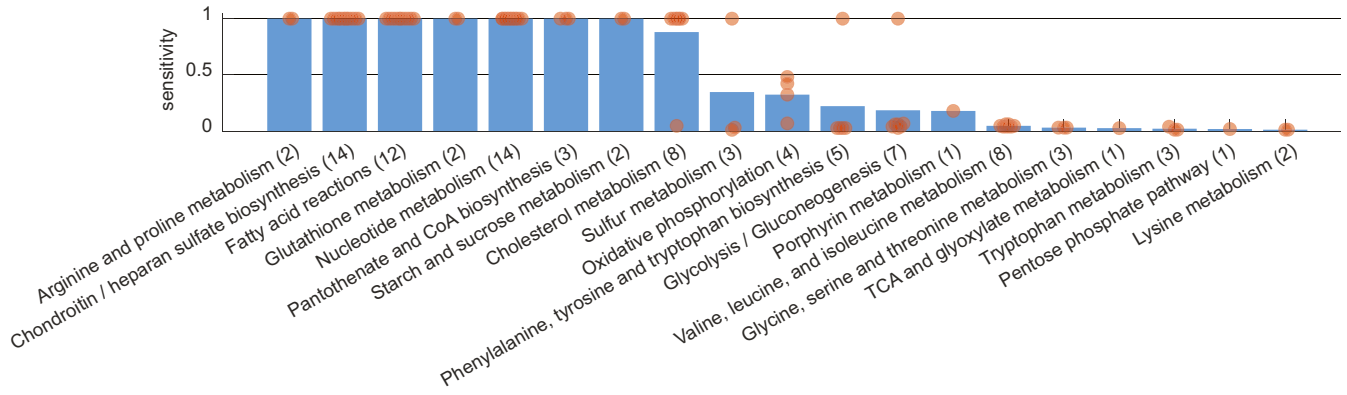


**Fig. 5.** Sensitivity of growth to perturbations in flux. The average sensitivity in different pathways (blue bars) to a small perturbation in flux for each reaction in the pathway (orange circles). Only reactions with detectable sensitivity (>0.01) were included in the analysis, and different reactions with the same gene associations were only counted once; the total number of reactions analyzed for each pathway is given in parenthesis. A total of 59 reactions had a strong effect (sensitivity > 0.5), and 36 reactions had modest effects (sensitivity between 0.01 and 0.5).

observed 2:1 ratio of exchange fluxes for glutamate and cystine compared with the 1:1 stoichiometry of the antiporter. Two of the excitatory amino acid transporters that are involved with glutamate transport (EAAT2 are EAAT3) are expressed in liver; however, these are ion-coupled importers that are not expected to excrete glutamate (58). One of the vesicular glutamate transporters (VGLUT3) is also expressed in liver, and it has been speculated that it may have a role in excretion of glutamate (59). However, a study that applied a VGLUT inhibitor to multiple cell lines found no significant reduction in extracellular glutamate levels, while inhibition with SSZ reduced glutamate markedly (60). It is therefore possible that glutamate is excreted through some heretofore unknown mechanism or transporter. The mitochondrial transporters are of great importance to understand cellular compartmentalization, but they are generally poorly characterized. Indeed, while mitochondrial uptake of glutamine is evident, the mitochondrial glutamine transporter has yet not been identified (61). The glutamate transporter, on the other hand, is known (62), and it has been speculated that instead of transporting glutamine directly, cells degrade it to glutamate in the intermembrane space by a glutaminase attached to the outside of the mitochondrial matrix, and then pump glutamate into the mitochondria (61). It would then be unclear why the mitochondria would not also take up cytosolic glutamate as the uptake of glutamate into the mitochondria—rather than excretion to the medium—would reduce the cells' demand for glutamine. One reason that this does not occur could be the aspartate–glutamate antiporter; in isolated mitochondria, glutamate uptake is accompanied by simultaneous release of aspartate (63), and accumulation of cytosolic aspartate may potentially prevent this option in living cells.

During the first hours of the experiment, amino acids appeared to be consumed at rates markedly higher than at later time points. Protein secretion is known to occur in liver cells (64, 65), and the addition of protein secretion provided our model with a sink for this. While it is possible that rapid protein secretion is a liver-specific phenotype, other cell lines may exhibit the same behavior, and this could potentially explain some of the divergence between observed amino acid uptake rates and the requirements for growth seen in other studies (3, 5). The analysis would have been compromised if the rapid and balanced phase were not studied in isolation, illustrating the importance of time-resolved metabolite measurements.

The pwFBA method that enabled identification of the growth phases constitutes a simplified form of a previous method (6) that was developed to study dioxic shifts in microbes, dynamic FBA (dFBA). Unlike dFBA, which divides time into thousands of slices, solving one FBA problem for each slice, the pwFBA method operates under the assumption that specific growth rate and exchange fluxes remain constant between each metabolic event and only solves a single FBA problem per growth phase. Unlike dFBA, it does not use rate of change of flux constraints or other forms of kinetic constraints. It is therefore well suited to for mapping out different growth phases with automatic calculation of growth rate, providing sanity checks on the estimated fluxes. However, for quantifying fluxes within an identified growth phase, the mLL method is preferred over pwFBA, as it allows estimation of fluxes and their confidence intervals directly from the data.

The fluxes calculated in this paper assumed that cells grow exponentially with constant specific exchange rates during each growth phase. The observed metabolite concentrations could potentially be consistent with cells growing with constantly decreasing specific growth rates and specific exchange fluxes, e.g., linear growth. However, for most conditions, this is not consistent with the measured cell counts. Despite substantial variability in internal fluxes, the major fluxes contributing to cytosolic glutamate metabolism are well characterized. Most of the biosynthetic fluxes had limited variability, which is expected since they depend linearly on the specific growth rate. There was also no variability for the predicted BCAA fluxes since BCAT is the only enzyme that degrades BCAAs, and its flux is thus directly linked to the measurements. Taken together, this translates to a high degree of certainty about the fluxes surrounding cytosolic glutamate pool. Another limitation was the fixed biomass composition that could not account for adaptations of the biomass to changes in growth conditions. It is, however, unlikely that biomass composition changes drastically; while in liver, one may expect glycogen content to be highly dynamic, less variability is expected for nucleotide and protein pools, which are important for the fate of glutamate.

Our analysis has been limited to in vitro grown liver cancer cells. This has the advantages that all metabolite changes can be attributed to the liver cancer cells. Of course, the nutritional context in vivo is more dynamic—supply of nutrients will be dependent on cancer tissue perfusion and the metabolism of neighboring cells. By using 6 mM glucose, instead of the 25 mM often used in cell culture, our cells experienced blood-like glucose levels. In addition, the depletion of nutrients in the medium may reflect some of the dynamics when cancer tissue perfusion is low.

The present study demonstrates how genome-scale metabolic models, together with a rigorous quantitative and time-resolved dataset, can provide an integrative view of metabolism of mammalian cells. The automatic compression and visualization of metabolic pathways using GEMpress has made the genome-wide scope manageable for interpretation. With these tools and methods, we have uncovered a mechanistic basis for the observed relation between glutamine uptake, glutamate excretion, and growth that allowed us to estimate the expected effect of several drug targets. We are therefore confident that this approach can be used more widely for hypothesis generation and testing concerning cancer metabolism in the future.



## Methods

**Cell Lines and Culture Conditions.** The human hepatocellular carcinoma cell line HepG2 was purchased from the ATTC were grown in culture medium consisting of the glucose-free version of DMEM (no. A14430; Gibco) supplemented with 10% FCS (article no. 10270106, batch 42F7565K), 6 mM glucose (or other levels as indicated in the text), 1.8 mM L-glutamine (25030-123; Gibco), and 100 U/mL penicillin and 100 μg/mL streptomycin (Gibco). Cells were kept at 5% $CO_2$, 37 °C, and 95% humidity. Cells were passaged to a maximum of 25 passages.

**Cell Counting.** To count the cells, cells were washed in phosphate-buffered saline (PBS) and were detached from the dish by adding 0.05% preheated trypsin-EDTA solution (Gibco). FCS-containing medium was added, and the cell suspension centrifuged at 1000 × *g* for 2 min. The supernatant was removed, and cells were resuspended in growth medium. The solution was passed several times through a pipet tip, to get a solution of single cells. Cell densities of cell suspensions were determined using a Bürker cell chamber (0.0025 $mm^2$; depth of chamber: 0.1 mm; Marienfeld Superior). Each cell suspension was counted twice.

**Protein Quantification.** The pellet obtained after centrifugation was taken up in a defined volume of medium, and a counting sample was taken. The remainder of the solution was then washed twice with PBS to remove residual proteins from the FCS and resuspended in PBS. Protein content was determined with a Pierce BCA Protein Assay Kit (ThermoScientific) according to the manufacturer's instructions.

**Medium Samples.** Samples were taken from the culture medium, aliquoted, instantly frozen in $N_2$ (liquid), and stored at −80 °C awaiting further analyses.

**Determination of Glucose and Pyruvate Concentrations.** Glucose and pyruvate concentrations were determined by high-performance liquid chromatography (HPLC). Medium samples were thawed on ice and underwent a perchloric acid (PCA)/potassium hydroxide (KOH) extraction and filtration to remove proteins: PCA was added to a final concentration of 3.5% (vol/vol), and samples were incubated on ice for 10 min. Then, 1/10 of volume of 5 M

KOH in 0.2 M 3-(*N*-morpholino)propanesulfonic acid was added, and samples were again incubated on ice for 10 min. Samples were centrifuged at maximum speed, and supernatant was filtered through a 0.22-μm Millex-GV polyvinylidene fluoride filter (Millipore); 50 μL of sample was injected on a Shimadzu HPLC with a Rezex ROA Organic Acid column and thermostated at 55 °C, and 5 mM $H_2SO_4$ was used as eluent. Glucose was detected by a refractive index detector, and pyruvate was detected by a ultraviolet detector. Concentrations were calculated based on a calibration curve and corrected for dilution by the PCA/KOH extraction.

**Determination of Amino Acid Concentrations.** Amino acid concentrations in the supernatant were determined according to the technique developed by Stein and Moore (66), involving derivatization with ninhydrine on a Biochrom 30+ amino acid analyser (Biochrom Ltd., Cambridge, UK). Amino acid concentrations were determined by comparison to calibration curves established using the same method.

**Enzymatic Determination of Lactate Concentrations.** Medium samples were thawed on ice. L-Lactate was measured by adding 20 μL of sample to 225 μL of buffer containing 440 mM glycine, 360 mM hydrazine, and 2.8 mM oxidized nicotinamide adenine dinucleotide ($NAD^+$). Baseline absorbance was recorded in a microplate spectrophotometer (Multiskan Go; ThermoScientific) at 340 nm and 37 °C. The reaction was started by adding 5 μL L-LDH (25 mg/5 mL; no. 101127876001; Roche). The increase in absorbance through formation of NADH was followed until the reaction had finished. $\Delta A_{340}$ between end and baseline was calculated for each incubation. After subtraction of the $\Delta A_{340}$ of the blanks, concentrations were calculated based on a calibration curve that was run in the same plate.

**SSZ Experiment.** SSZ was purchased from Sigma and dissolved in sterile 1 M $NH_4OH$. The final concentration of $NH_4OH$ was 2 mM. Cells were grown in different concentrations of SSZ (0, 0.1, and 0.2 mM); 0 mM cultures were grown in the presence of the $NH_4OH$ solvent. Cells were counted at four time points (0, 24, 45, and 68 h), but the last time point was excluded from the analysis since it occurred after glucose depletion. A linear function of time (t) with growth (μ) and dose (d) as parameters was fitted to the logarithmized cell counts (y), $y = t\cdot(\mu_0 - \mu_d\cdot d) + \text{intercept}$. For metabolites, a linear function was fitted to the metabolite concentrations. The *P* values for the terms were calculated using the linear model fitting (fitlm function) in a scientific programming platform (MATLAB; MathWorks, Inc.); only the *P* value for the dose term is reported in Fig. 4.

**Genome-Scale Metabolic Model.** The model was based on the Human Metabolic Reaction database HMR 2.0, a generic genome-scale metabolic model (23), from which reactions without support in RNA-seq data from HepG2 cells (67) were removed, based on a previous analysis (24). The biomass equation was updated (*SI Appendix, Supplementary Methods* and Tables S1–S4) and included the amino acid composition, which was estimated from a proteomics dataset of HepG2 cells (26) and the amino acid frequency of the proteins from an online database (68). Around 10% of the biomass consists of metabolites, and the concentrations of these were taken from a metabolomics study on iBMK cells (40). The maintenance energy expenditure (1 mmol ATP $h^{-1}$ $gdw^{-1}$) and growth-associated energy expenditure (48 mmol ATP/gdw) were estimated from a literature survey of reported values from various mammalian cell types (*SI Appendix, Supplementary Methods* and Table S5) and was consistent with ATP expenditure estimated from protein turnover (*SI Appendix*, Fig. S10). Additional manual curation of the model was performed (*SI Appendix, Supplementary Methods* and Tables S6–S9).

**FBA.** FBA was carried out using the RAVEN Toolbox (69). When indicated, unique flux solutions were identified using the parsimonious FBA method (70). Briefly, the list of reactions included in the model are transformed into a stoichiometric matrix (*S*) with columns corresponding to reactions with stoichiometric coefficients of the participating metabolites (rows). Under the assumption of steady state, a flux distribution (**v**), expressed in millimoles per gram dry cell weight per hour, is sought that maximizes flux through the biomass synthesis reaction, which is expressed as a weighted (**c**) maximization problem,

$$\begin{gathered}\mathbf{Sv} = 0\\ \max\ \mathbf{c}^T\mathbf{v}\\ \min|\mathbf{v}|\end{gathered}$$

When indicated, a second optimization, i.e., pwFBA, is run to remove loops and reduce large fluxes. The absolute value of all fluxes is minimized, while preserving the maximum flux through the objective function.

**FVA.** To find the range of possible metabolic fluxes, each flux is minimized and maximized in turn, as previously described (71). For the FVA used in Fig. 3*A*, the variability was reported for groups of reactions with the same function, e.g., transport of glutamate; this was calculated by maximizing/minimizing the sum of flux, taking stoichiometry into account; additionally, the growth rate was constrained to the observed level with a 1% tolerance to account for uncertainties.

**pwFBA.** A set of ordinary differential equations (ODEs) were set up to describe how cell dry weight (*X*) and metabolite concentrations (*S*) changes over time (*t*), as a function of the specific growth rate (μ), the specific exchange fluxes (*f*), and spontaneous degradation rates (*r*),

$$\begin{aligned}\frac{dX}{dt} &= \mu X\\ \frac{dS}{dt} &= fX - rS.\end{aligned} \qquad [1]$$

All metabolites were assumed to be stable ($r = 0$), apart from glutamine, which is known to undergo spontaneous degradation forming ammonia and 5-oxoproline (72), which was modeled by first-order kinetics ($r = 0.0023\ h^{-1}$). The experimentally observed cell dry weight and metabolite concentrations at time 0 were used as boundary condition. FBA was used to calculate the maximum attainable μ from f. The ODE problem was solved for the time intervals between each experimental sampling point after which the medium volume was adjusted for the amount removed for the sample. When metabolite concentrations reached predefined thresholds a new set of specific exchange fluxes (f) was used, and μ was recalculated using FBA. A typical threshold was 0 mM, signifying metabolite depletion. The exchange fluxes were manually fitted until there was agreement between predicted and experimentally determined cell counts and metabolite concentrations. To semiautomate this task, tentative timepoints for the growth phase transitions were identified by piecewise linear regression of the log-transformed cell count data. Tentative fluxes were estimated and fine-tuned using least squares fitting to the metabolite concentration data using an analytical solution of the ODE system. However, since these fits did not take all of the constraints used by the ODE formulation into consideration, e.g., the growth-effects of the fluxes, the estimated fluxes were manually adjusted for agreement with the data.

**mLL Estimates of Fluxes under Steady-State Conditions.** To quantify the fluxes under the identified steady state condition, parameter values were fitted to the analytical solution of Eq. **1** (model),

$$\begin{aligned}X(t) &= X_0 e^{\mu t}\\ S(t) &= S_0 + \frac{f}{\mu}X_0\left(e^{\mu t} - 1\right)'\end{aligned}$$

assuming exponential growth ($\mu$) and constant specific flux (*f*), and neglecting spontaneous degradation, which was estimated to constitute <5% of the glutamine flux at this time (*SI Appendix*, Fig. S3). Changes in medium volume due to repeated sampling were accounted for by segmenting the model into time intervals where volume was constant. The estimates of initial concentrations, fluxes, and specific growth rate, as well as the SD ($\sigma$) for each observable, were estimated using the mLL formalism, as

$$\begin{gathered}e = model - data\\ mLL = \sum -\frac{\ln 2\pi}{2} - \frac{\ln \sigma^2}{2} - \frac{1}{2}\left(\frac{e^2}{\sigma^2}\right)\\ \max mLL.\end{gathered}$$

The 95% CI was estimated by identifying parameter values with mLL estimates equal to the optimum plus the inverse $\chi^2$ distribution with one degree of freedom and 95% probability. Each flux was fitted independently using this method, resulting in multiple growth estimates with corresponding CIs. The mean of the growth estimates and minimum and maximum of the CIs were reported. To improve power the cell count, data from 6 and 22 mM conditions were pooled, as there was no apparent difference in growth rate between these conditions, and data from 55 and 48 h were pooled for the 0 mM condition, as there was no apparent increase in growth after 48 h. The concentration of asparagine was below the detection limit and was excluded from the analysis.

**GEMpress and Shortest-Path Method.** GEMpress takes a flux distribution as input and lumps fluxes in such a way that all metabolites that are not branch points in the metabolic network are canceled out (*SI Appendix, Supplementary Methods*). In brief, the shortest path between sets of metabolites was calculated with a breadth-first search algorithm using the bipartite graph of the GEMpress-reduced metabolic network as input. The weight for cofactors was set to zero to avoid shortcuts through metabolites such as ATP. The algorithm returns a list of metabolites and reactions that are involved in the shortest path.

**Sensitivity Analysis.** The sensitivity of metabolic fluxes was investigated by calculating their elasticities (E), i.e., percentage change in maximum growth rate ($\Delta\mu$) from percentage change in flux ($\Delta f$): $E = \frac{\Delta\mu}{\Delta f}$. To prevent infeasible changes in flux, the uptake fluxes were relaxed to allow lower than observed values.

**Data Availability Statement.** The raw data are available online in the repository FAIRDOMHub (73) (DOI: 10.15490/fairdomhub.1.investigation.369.1). A formatted version of the data is available in Dataset S1. The model and the source code for the computational methods are available at GitHub (https://github.com/SysBioChalmers/LiverCellMetabolismSimulation).

**ACKNOWLEDGMENTS.** We thank Elias Björnson and Joep Vanlier for valuable comments. We acknowledge funding from the ERASysAPP (ERA-Net for Systems Biology) project IMOMESIC (Integrating Modelling of Metabolism and Signalling towards an Application in Liver Cancer), which received funding from The Swedish Research Council, Västra Götaland Regional Council and ZonMw (The Netherlands Organisation for Health Research and Development), and the Deutsche Forschungsgemeinschaft. Funding from the Knut and Alice Wallenberg Foundation is also acknowledged.

1. D. Hanahan, R. A. Weinberg, Hallmarks of cancer: The next generation. *Cell* **144**, 646–674 (2011).
2. A. M. Hosios *et al*., Amino acids rather than glucose account for the majority of cell mass in proliferating mammalian cells. *Dev. Cell* **36**, 540–549 (2016).
3. S. C. Dolfi *et al*., The metabolic demands of cancer cells are coupled to their size and protein synthesis rates. *Cancer Metab.* **1**, 20 (2013).
4. D. R. Wise, C. B. Thompson, Glutamine addiction: A new therapeutic target in cancer. *Trends Biochem. Sci.* **35**, 427–433 (2010).
5. D. C. Zielinski *et al*., Systems biology analysis of drivers underlying hallmarks of cancer cell metabolism. *Sci. Rep.* **7**, 41241 (2017).
6. M. Jain *et al*., Metabolite profiling identifies a key role for glycine in rapid cancer cell proliferation. *Science* **336**, 1040–1044 (2012).
7. A. Stepulak, R. Rola, K. Polberg, C. Ikonomidou, Glutamate and its receptors in cancer. *J. Neural. Transm.* **121**, 933–944 (2014).
8. M. Newland, P. F. Greenfield, S. Reid, Hybridoma growth limitations: The roles of energy metabolism and ammonia production. *Cytotechnology* **3**, 215–229 (1990).
9. W. Palm, C. B. Thompson, Nutrient acquisition strategies of mammalian cells. *Nature* **546**, 234–242 (2017).
10. J. Fan *et al*., Glutamine-driven oxidative phosphorylation is a major ATP source in transformed mammalian cells in both normoxia and hypoxia. *Mol. Syst. Biol.* **9**, 712 (2013).
11. J. Fan *et al*., Quantitative flux analysis reveals folate-dependent NADPH production. *Nature* **510**, 298–302 (2014).
12. J. D. Orth, I. Thiele, B. Ø. O. Palsson, What is flux balance analysis? *Nat. Biotechnol.* **28**, 245–248 (2010).
13. R. Agren *et al*., Identification of anticancer drugs for hepatocellular carcinoma through personalized genome-scale metabolic modeling. *Mol. Syst. Biol.* **10**, 721 (2014).
14. N. E. Lewis, H. Nagarajan, B. O. Palsson, Constraining the metabolic genotype-phenotype relationship using a phylogeny of in silico methods. *Nat. Rev. Microbiol.* **10**, 291–305 (2012).
15. A. Nilsson, A. Mardinoglu, J. Nielsen, Predicting growth of the healthy infant using a genome scale metabolic model. *NPJ Syst. Biol. Appl.* **3**, 3 (2017).
16. A. Nilsson, E. Björnson, M. Flockhart, F. J. Larsen, J. Nielsen, Complex I is bypassed during high intensity exercise. *Nat. Commun.* **10**, 5072 (2019).
17. V. S. Martínez *et al*., Flux balance analysis of CHO cells before and after a metabolic switch from lactate production to consumption. *Biotechnol. Bioeng.* **110**, 660–666 (2013).
18. A. Nilsson, J. Nielsen, Genome scale metabolic modeling of cancer. *Metab. Eng.* **43**, 103–112 (2017).
19. A. Nilsson, J. R. Haanstra, B. Teusink, J. Nielsen, Metabolite depletion affects flux profiling of cell lines. *Trends Biochem. Sci.* **43**, 395–397 (2018).
20. K. A. Hoadley *et al*.; Cancer Genome Atlas Research Network, Multiplatform analysis of 12 cancer types reveals molecular classification within and across tissues of origin. *Cell* **158**, 929–944 (2014).
21. M. O. Yuneva *et al*., The metabolic profile of tumors depends on both the responsible genetic lesion and tissue type. *Cell Metab.* **15**, 157–170 (2012).
22. S. Rodríguez-Enríquez *et al*., Canonical and new generation anticancer drugs also target energy metabolism. *Arch. Toxicol.* **88**, 1327–1350 (2014).
23. A. Mardinoglu *et al*., Genome-scale metabolic modelling of hepatocytes reveals serine deficiency in patients with non-alcoholic fatty liver disease. *Nat. Commun.* **5**, 3083 (2014).
24. P. Ghaffari *et al*., Identifying anti-growth factors for human cancer cell lines through genome-scale metabolic modeling. *Sci. Rep.* **5**, 8183 (2015).
25. H. Ogata *et al*., KEGG: Kyoto Encyclopedia of Genes and Genomes. *Nucleic Acids Res.* **27**, 29–34 (1999).
26. J. R. Wiśniewski, A. Vildhede, A. Norén, P. Artursson, In-depth quantitative analysis and comparison of the human hepatocyte and hepatoma cell line HepG2 proteomes. *J. Proteomics* **136**, 234–247 (2016).
27. R. Mahadevan, J. S. Edwards, F. J. Doyle, 3rd, Dynamic flux balance analysis of diauxic growth in Escherichia coli. *Biophys. J.* **83**, 1331–1340 (2002).
28. U. Hofmann *et al*., Identification of metabolic fluxes in hepatic cells from transient 13C-labeling experiments: Part I. Experimental observations. *Biotechnol. Bioeng.* **100**, 344–354 (2008).
29. S. Tardito *et al*., Glutamine synthetase activity fuels nucleotide biosynthesis and supports growth of glutamine-restricted glioblastoma. *Nat. Cell Biol.* **17**, 1556–1568 (2015).
30. C. Kreutz, A. Raue, J. Timmer, Likelihood based observability analysis and confidence intervals for predictions of dynamic models. *BMC Syst. Biol.* **6**, 120 (2012).
31. Y. Dai, J. Cui, P. Gan, W. Li, Downregulation of tetrahydrobiopterin inhibits tumor angiogenesis in BALB/c-nu mice with hepatocellular carcinoma. *Oncol. Rep.* **36**, 669–675 (2016).
32. M. Uhlen *et al*., A pathology atlas of the human cancer transcriptome. *Science* **357**, eaan2507 (2017).
33. W. Liu, C. N. Hancock, J. W. Fischer, M. Harman, J. M. Phang, Proline biosynthesis augments tumor cell growth and aerobic glycolysis: Involvement of pyridine nucleotides. *Sci. Rep.* **5**, 17206 (2015).
34. S. Raffel *et al*., BCAT1 restricts αKG levels in AML stem cells leading to IDHmut-like DNA hypermethylation. *Nature* **551**, 384–388 (2017).
35. L. Dang *et al*., Cancer-associated IDH1 mutations produce 2-hydroxyglutarate. *Nature* **462**, 739–744 (2009).
36. M. Tönjes *et al*., BCAT1 promotes cell proliferation through amino acid catabolism in gliomas carrying wild-type IDH1. *Nat. Med.* **19**, 901–908 (2013).
37. M. Lo, Y. Z. Wang, P. W. Gout, The x(c)- cystine/glutamate antiporter: A potential target for therapy of cancer and other diseases. *J. Cell. Physiol.* **215**, 593–602 (2008).
38. T. Shlomi, T. Benyamini, E. Gottlieb, R. Sharan, E. Ruppin, Genome-scale metabolic modeling elucidates the role of proliferative adaptation in causing the Warburg effect. *PLoS Comput. Biol.* **7**, e1002018 (2011).
39. P. Koppula, Y. Zhang, J. Shi, W. Li, B. Gan, The glutamate/cystine antiporter SLC7A11/xCT enhances cancer cell dependency on glucose by exporting glutamate. *J. Biol. Chem.* **292**, 14240–14249 (2017).
40. J. O. Park *et al*., Metabolite concentrations, fluxes and free energies imply efficient enzyme usage. *Nat. Chem. Biol.* **12**, 482–489 (2016).
41. B. Bayram, G. Rimbach, J. Frank, T. Esatbeyoglu, Rapid method for glutathione quantitation using high-performance liquid chromatography with coulometric electrochemical detection. *J. Agric. Food Chem.* **62**, 402–408 (2014).
42. S. C. Lu *et al*., Role of two recently cloned rat liver GSH transporters in the ubiquitous transport of GSH in mammalian cells. *J. Clin. Invest.* **97**, 1488–1496 (1996).
43. F. P. Kuhajda, Fatty-acid synthase and human cancer: New perspectives on its role in tumor biology. *Nutrition* **16**, 202–208 (2000).
44. J. Fan, J. J. Kamphorst, J. D. Rabinowitz, T. Shlomi, Fatty acid labeling from glutamine in hypoxia can be explained by isotope exchange without net reductive isocitrate dehydrogenase (IDH) flux. *J. Biol. Chem.* **288**, 31363–31369 (2013).
45. H. Kinoshita *et al*., Cystine/glutamic acid transporter is a novel marker for predicting poor survival in patients with hepatocellular carcinoma. *Oncol. Rep.* **29**, 685–689 (2013).
46. J. K. M. Lim *et al*., Cystine/glutamate antiporter xCT (SLC7A11) facilitates oncogenic RAS transformation by preserving intracellular redox balance. *Proc. Natl. Acad. Sci. U.S.A.* **116**, 9433–9442 (2019).
47. S. J. Dixon *et al*., Pharmacological inhibition of cystine-glutamate exchange induces endoplasmic reticulum stress and ferroptosis. *eLife* **3**, e02523 (2014).
48. K. Ogihara *et al*., Sulfasalazine could modulate the CD44v9-xCT system and enhance cisplatin-induced cytotoxic effects in metastatic bladder cancer. *Cancer Sci.* **110**, 1431–1441 (2019).
49. D. H. Kim, M. D. Abdullah, and S. J. Lee, Mechanisms of growth inhibition by sulfasalazine and erastin in hepatocellular carcinoma cell lines. *Yakhak Hoeji* **63**, 152–159 (2019).
50. P. Nahon *et al*., Identification of serum proton NMR metabolomic fingerprints associated with hepatocellular carcinoma in patients with alcoholic cirrhosis. *Clin. Cancer Res.* **18**, 6714–6722 (2012).
51. G. Ollenschläger *et al*., Plasma glutamate–A prognostic marker of cancer and of other immunodeficiency syndromes? *Scand. J. Clin. Lab. Invest.* **49**, 773–777 (1989).
52. D. A. MacIntyre *et al*., Serum metabolome analysis by 1H-NMR reveals differences between chronic lymphocytic leukaemia molecular subgroups. *Leukemia* **24**, 788–797 (2010).
53. V. Hack *et al*., Elevated venous glutamate levels in (pre)catabolic conditions result at least partly from a decreased glutamate transport activity. *J. Mol. Med.* **74**, 337–343 (1996).
54. C. Wahl, S. Liptay, G. Adler, R. M. Schmid, Sulfasalazine: A potent and specific inhibitor of nuclear factor kappa B. *J. Clin. Invest.* **101**, 1163–1174 (1998).

55. C. Chidley, H. Haruki, M. G. Pedersen, E. Muller, K. Johnsson, A yeast-based screen reveals that sulfasalazine inhibits tetrahydrobiopterin biosynthesis. *Nat. Chem. Biol.* **7**, 375–383 (2011).
56. Y. Song *et al*., Sulfasalazine attenuates evading anticancer response of CD133-positive hepatocellular carcinoma cells. *J. Exp. Clin. Cancer Res.* **36**, 38 (2017).
57. F. Wada *et al*., High expression of CD44v9 and xCT in chemoresistant hepatocellular carcinoma: Potential targets by sulfasalazine. *Cancer Sci.* **109**, 2801–2810 (2018).
58. Y. Kanai *et al*., The SLC1 high-affinity glutamate and neutral amino acid transporter family. *Mol. Aspects Med.* **34**, 108–120 (2013).
59. R. T. Fremeau *et al*., The identification of vesicular glutamate transporter 3 suggests novel modes of signaling by glutamate. *Proc. Natl. Acad. Sci. U.S.A.* **99**, 14488–14493 (2002).
60. M. K. Sharma, E. P. Seidlitz, G. Singh, Cancer cells release glutamate via the cystine/glutamate antiporter. *Biochem. Biophys. Res. Commun.* **391**, 91–95 (2010).
61. M. Scalise, L. Pochini, M. Galluccio, L. Console, C. Indiveri, Glutamine transport and mitochondrial metabolism in cancer cell growth. *Front. Oncol.* **7**, 306 (2017).
62. G. Fiermonte *et al*., Identification of the mitochondrial glutamate transporter. Bacterial expression, reconstitution, functional characterization, and tissue distribution of two human isoforms. *J. Biol. Chem.* **277**, 19289–19294 (2002).
63. Z. Kovačević, The pathway of glutamine and glutamate oxidation in isolated mitochondria from mammalian cells. *Biochem. J.* **125**, 757–763 (1971).
64. P. Tessari *et al*., Impairment of albumin and whole body postprandial protein synthesis in compensated liver cirrhosis. *Am. J. Physiol. Endocrinol. Metab.* **282**, E304–E311 (2002).
65. M. B. Caruso *et al*., Proteomic analysis of the secretome of HepG2 cells indicates differential proteolytic processing after infection with dengue virus. *J. Proteomics* **151**, 106–113 (2017).
66. S. Moore, D. H. Spackman, W. H. Stein, Chromatography of amino acids on sulfonated polystyrene resins: An improved system. *Anal. Chem.* **30**, 1185–1190 (1958).
67. L. Fagerberg *et al*., Contribution of antibody-based protein profiling to the human Chromosome-centric Proteome Project (C-HPP). *J. Proteome Res.* **12**, 2439–2448 (2013).
68. A. Bateman *et al*.; The UniProt Consortium, UniProt: The universal protein knowledgebase. *Nucleic Acids Res.* **45**, D158–D169 (2017).
69. R. Agren *et al*., The RAVEN toolbox and its use for generating a genome-scale metabolic model for Penicillium chrysogenum. *PLoS Comput. Biol.* **9**, e1002980 (2013).
70. N. E. Lewis *et al*., Omic data from evolved E. coli are consistent with computed optimal growth from genome-scale models. *Mol. Syst. Biol.* **6**, 390 (2010).
71. R. Mahadevan, C. H. Schilling, The effects of alternate optimal solutions in constraint-based genome-scale metabolic models. *Metab. Eng.* **5**, 264–276 (2003).
72. S. S. Ozturk, B. O. Palsson, Chemical decomposition of glutamine in cell culture media: Effect of media type, pH, and serum concentration. *Biotechnol. Prog.* **6**, 121–128 (1990).
73. K. Wolstencroft *et al*., FAIRDOMHub: A repository and collaboration environment for sharing systems biology research. *Nucleic Acids Res.* **45**, D404–D407 (2017).